MINI-RF S-BAND RADAR OBSERVATIONS OF THE MOON AS A FUNCTION OF LOCAL INCIDENCE ANGLE. C. I. Fassett[1], E. G. Rivera-Valentín[1], G. W. Patterson[1], J. T. S. Cahill[1], G. A. Morgan[2], C. D. Neish[2,3], A. K. Virkki[4], P. A. Taylor[5], M. C. Nolan[6], M. Slade[7], S. S. Bhiravarasu[8]. [1]JHU-Applied Physics Laboratory (caleb.fassett@jhuapl.edu), [2]PSI, [3]Dept. of Earth Sciences, Univ. of Western Ontario, [4]University of Helsinki, [5]NRAO & Green Bank Observatory, [6]LPL, University of Arizona, [7]NASA JPL/Caltech, [8]Space Applications Centre, ISRO, Ahmedabad, India.

Introduction: The Miniature Radio Frequency (Mini-RF) instrument on Lunar Reconnaissance Orbiter (LRO) is a Synthetic Aperture Radar designed in a hybrid dual-polarimetric architecture that transmits a circularly polarized signal to the lunar surface and receives the horizontal and vertical linear polarizations [1]. Monostatic radar data was collected in this mode until 26 Dec. 2010, when the transmitter ceased to operate. Since 2011, bistatic observations in S-Band and X-Band have been conducted by transmitting from ground-based facilities and receiving scattered light from the lunar surface onboard LRO [2]. The received radar signal from Mini-RF is represented using the four Stokes parameters (S_{1-4}), which can be combined to derive metrics for lunar surface properties.

Returned radar power and polarimetry are both dependent on the local incidence angle (i), where i is the angle between the radar illumination and a vector drawn perpendicular to the target's surface (surface normal vector) taking topography into account (i=0°: direct illumination; i=90°: grazing). At low incidence, specular returns dominate, whereas diffuse scattering becomes more important at high incidence angles [e.g., 3-5]. Although the importance of this effect has been recognized in the Mini-RF data [6-8], a global analysis was not easily accessible because a backplane with i was not available for the monostatic data.

Here, we examine the Mini-RF S-band behavior as a function of local incidence angle after registering the monostatic data to a SLDEM [9] (LOLA at high latitudes) topographic reference frame. We also make a similar calculation for the Mini-RF S-band bistatic data, whose processing chain [10] already provides a local incidence angle of each pixel.

Methods: The PDS-released Mini-RF monostatic dataset is imperfectly tied to SLDEM for two reasons. First, the data were projected onto a spherical Moon, so that pixels were not orthorectified [e.g., 7]. Second, and more challenging, is that there are known positional offsets along-track [11] that appear to be traced to the VEXCEL processing pipeline. For non-polar data, we addressed these issues with a processing chain in USGS ISIS and python/numpy by (i) taking the Level 1 (un-map-projected) dataset and attaching local SLDEM-derived topography as a shape model with *spiceinit*; (ii) calculating i given the monostatic radar geometry with

phocube; (iii) creating an initial guess of a synthetic S_1 based on a model for the empirical relationship between S_1 and i, using *fx*; (iv) applying a cross-correlation image registration algorithm [12] to calculate a linear shift (in image space, not map space) between the observed S_1 and synthetic S_1; (v) shifting the data by the calculated offset and then map-projecting and orthorectifying S_1-S_4, and attaching an i backplane. This process worked for 98% of the global, non-polar data. A portion of the monostatic dataset near the poles already had been seleno-referenced [e.g., 13], so for that data, step iii was replaced by tying S_1 to existing controlled S_1 mosaics rather than a model of S_1.

We binned the Mini-RF data as a function of local incidence angle into bins of 25000 pixels for each collect. Because the geometry of Mini-RF monostatic data acquisitions were typically fixed relative to the surface, the distribution of data is centered on 49°. For the Mini-RF bistatic data, greater variability exists in the acquisition geometry, so there is a broader range of incidence angles. S_1 was normalized based on the median of the given collect to 44-54° for the monostatic data and to 35-63° for the bistatic data.

Observations and Analysis: Figures 1a and 1c illustrate the relationship between local incidence angle i and normalized S_1. The observed increase in S_1 in the Mini-RF dataset appears generally consistent with expectations from ground-based observations [3-4]. Received power has an approximately $(\cos(i))^n$ dependence for $i \gtrsim 35°$, with $n \sim 1$–3, and a power-law dependence in the specular regime below $\sim 35°$. Differences between the behavior of the monostatic and bistatic data at high incidence (>60°) may be because of (a) the effective noise floor of the monostatic data, and (b) the non-exclusion of areas of true radar shadow in bistatic data, which become increasingly common at high incidence angles.

There is also a strong correlation seen in monostatic and bistatic data between local incidence and CPR (Fig. 1b/d). This is likely because at low incidence angles single bounces and low CPR (trending to ~ 0 in the limit), are favored. The occasional higher values seen at low incidence, especially in the monostatic data, may be a result of very rough and/or geometrically complex surfaces, or could be an uncorrected instrumental effect (leakage between polarization channels). At more

grazing incidence angles multiple bounces and higher CPR are observed (trending to ~1). The very strong influence of local incidence angle on CPR means that geologic interpretations with it need to consider topography carefully, as has been emphasized in the past [5-8].

References: [1] Nozette, S. et al. (2010), *Space Sci. Rev. 150,* 285–302. [2] Patterson, G.W. et al. (2017) *Icarus, 283*, 2–19. [3] Hagfors, T. (1970), *Radio Sci., 5*, 189–227. [4] Thompson, T. W. et al. (2011), *JGR., 116,* 10.1029/2009JE003368. [5] Fa, W. et al. (2011), *JGR, 116,* 10.1029/2010JE003649. [6] Fa, W. and Cai, Y. (2013), *JGR, 118*, 1582–1608. [7] Eke, V.R. et al. (2014), *Icarus, 241*, 66–78. [8] Virkki, A.K. & Bhiravarasu, S.S. (2019), *JGR, 124*, 3025–3040. [9] Barker, M.K. et al. (2016), *Icarus, 273*, 346–355. [10] Turner, F.S. et al. (2019), *49th Planetary Data Wkshp,* 7075. [11] Harris, C.P. et al. (2022), *LPSC 53,* 2856. [12] https://github.com/keflavich/image_registration. [13] Kirk R. L. et al. (2013), *LPSC 44*, 2920.
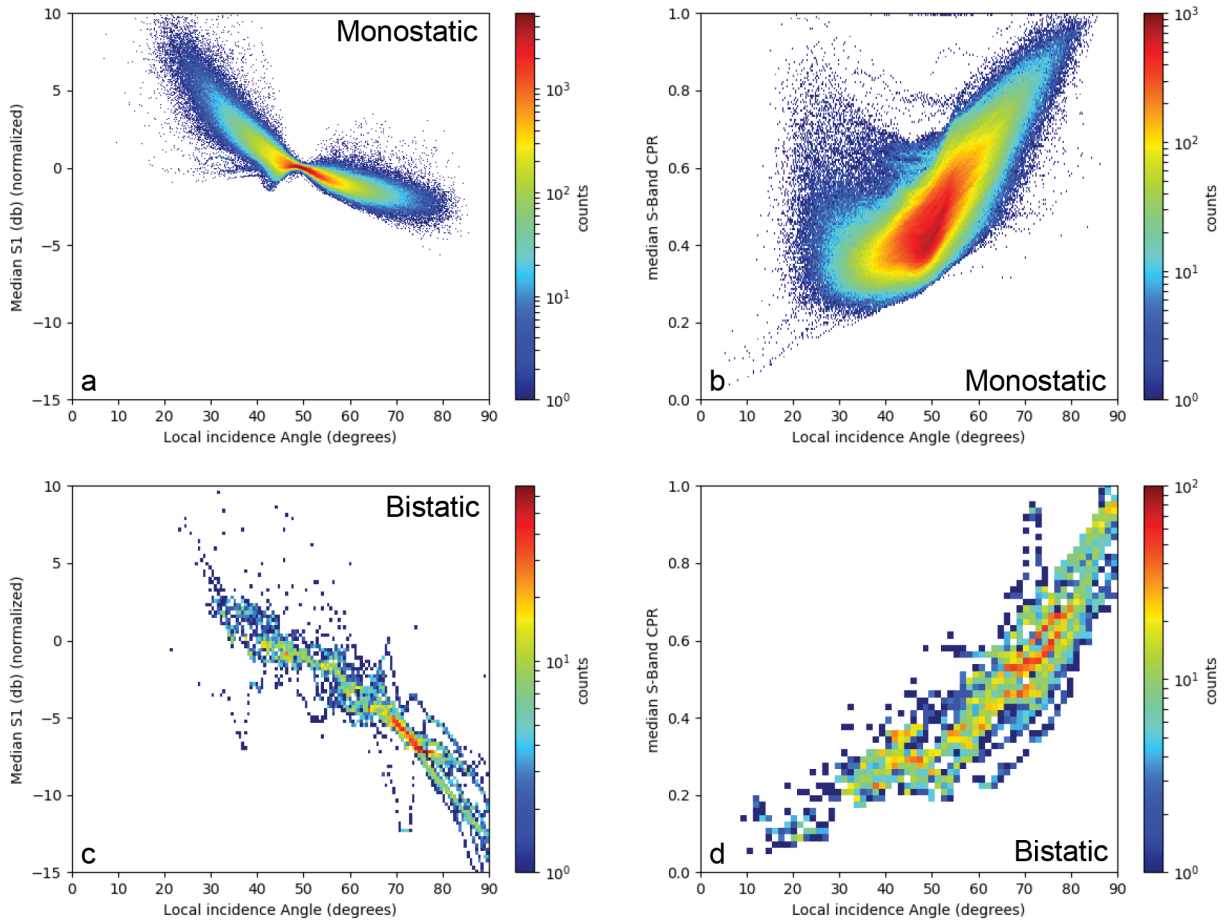

Figure 1. The observed median S_1 (total power, normalized) and CPR for (a and b) monostatic and (c and d) bistatic Mini-RF observations. The underlying dataset are calculated medians in (i, $S_{1-normalized}$) or (i,CPR) bins of 25000 pixels in each collect; the data are then combined in the 2d histograms that are shown. There is limited monostatic data at angles below ~20° or above ~80° because of the nominal observation geometry of the monostatic data at 49° combined with the topographic slope distribution on the Moon.